

GhostImage: Perception Domain Attacks against Vision-based Object Classification Systems

Yanmao Man
University of Arizona

Ming Li
University of Arizona

Ryan Gerdes
Virginia Tech

ABSTRACT

In vision-based object classification systems, imaging sensors perceive the environment and then objects are detected and classified for decision-making purposes. Vulnerabilities in the perception domain enable an attacker to inject false data into the sensor which could lead to unsafe consequences. In this work, we focus on camera-based systems and propose GhostImage attacks, with the goal of either creating a fake perceived object or obfuscating the object's image that leads to wrong classification results. This is achieved by remotely projecting adversarial patterns into camera-perceived images, exploiting two common effects in optical imaging systems, namely lens flare/ghost effects, and auto-exposure control. To improve the robustness of the attack to channel perturbations, we generate optimal input patterns by integrating adversarial machine learning techniques with a trained end-to-end channel model. We realize GhostImage attacks with a projector, and conducted comprehensive experiments, using three different image datasets, in indoor and outdoor environments, and three different cameras. We demonstrate that GhostImage attacks are applicable to both autonomous driving and security surveillance scenarios. Experiment results show that, depending on the projector-camera distance, attack success rates can reach as high as 100%.

KEYWORDS

Sensor Attacks, Adversarial Examples, Autonomous Systems

1 INTRODUCTION

Object detection and classification are widely adopted in autonomous systems, such as autonomous vehicles [78–80] and drones [1, 70], as well as surveillance systems, such as smart home monitoring systems [2, 23]. Such systems typically first perceive the surrounding environment via sensors (e.g., cameras, radars, LiDARs) that convert analog signal into digital data, and then try to understand it using object detectors and classifiers (e.g., recognizing traffic signs or home intrusion), based on which they make decisions and interact with the environment (e.g., a car decelerates, system raises an alarm). However, such technologies have not been fully accepted by the public because of safety and security concerns [8, 39, 90].

While attack surfaces in the cyber/digital domain have been widely studied [14, 16, 43, 58], vulnerabilities in the perception domain are less well-known. Perception is the first and critical step in the decision-making pipeline. If the sensors are compromised, false data can be injected, which could lead to incorrect decisions and actions. Recent works have demonstrated such false data injection via either electromagnetic interference [65], lasers [74], or acoustic waves [71], etc. Sensor attacks in the perception domain alter the data at the source, hence bypassing traditional cyber defenses (such as crypto-based authentication or access control), which are much



(a) Projector off

(b) Projector on

Figure 1: A STOP sign image was injected into a camera by a projector, which was detected by YOLOv3 [61].

harder to defend against [21, 89]. Such attacks are also remote and do not need to physically access/modify existing devices or objects.

Recently, several sensor attacks against autonomous vehicles have been proposed, including camera attacks [59, 90], and LiDAR attacks [11, 59, 67]. Different from vision-based imaging systems, LiDARs are mainly used for obstacle detection and ranging. LiDAR attacks are relatively easier to carry out because in order to create a fake object, the attacker could directly inject laser pulses. Also, LiDAR is not as widely adopted as cameras. For example, Tesla cars are not equipped with LiDARs [78]. Camera-based image classification systems, on the other hand, are more common but they are generally harder to spoof because the attacker cannot block the target object (otherwise it becomes trivial), and has to carefully control the injection intensity so as not to blind the camera. Limited existing camera attacks' goal was to blind the cameras (denial-of-service), instead of spoofing object detection or classification [59, 90]. Also, they can be easily detected (e.g., by tampering detection [62]), and then mitigated (e.g., by sensor fusion [34]).

In this work, we consider attacks that aim to spoof a vision-based image classification system, by remotely injecting light interference into a camera without disabling it, so as to cause incorrect classification or detection results. There are two different attack objectives: *Creation attacks* which creates a fake object (e.g., a STOP sign) in the perceived image, and *obfuscation attacks*, in which the image of an existing object is obfuscated into another attacker-chosen object (e.g., changing a STOP sign to a YIELD sign).

Due to optical principles, directly injecting light into the camera is not effective to create an image. Instead, we propose to exploit two common effects in optical imaging systems, *lens flare effects* and *exposure control*. The former is caused by the imperfection of lenses, among which light beams are refracted and also reflected multiple times, hence polygon-shape artifacts (a.k.a., *ghosts*) appear on images [26, 91]. Since ghosts and their light sources usually appear at different locations, the attacker can overlap the ghosts with the target object's image without blocking it by the light source. Auto exposure control is commonly equipped in cameras, by which

exposure can be adjusted so that images look more natural. The attacker can leverage this to make the background darker and the ghosts brighter, so as to increase attack success rates. Fig. 1 presents an example of a creation attack, where we used a projector to inject an image of a STOP sign in a ghost, which is detected and classified as a STOP sign by YOLOv3 [61], a state-of-the-art object detector.

Theoretically, arbitrary image patterns can be injected into the ghosts. However, it is challenging to practically and precisely control the ghosts in terms of their resolutions and positions in images. Hence, we propose an empirical projector-camera channel model that predicts the resolution of the injected patterns in ghosts, as well as the location of ghosts, given the relative positions of the projector and the camera in the real-world. Experimental results show that at short distances, the attack success rates could be as high as 100%, but at longer distances, the rates decreased to 40%. This is because at long distances, ghost resolutions are low, whose patterns could not be recognized by the image classifier.

To improve the robustness of GhostImage attacks (especially at lower resolutions), we assume that the attacker possesses the knowledge about the image classification algorithm, based on which the attacker formulates an optimization problem to find those optimal patterns in varying resolutions that can be recognized by the image classifier as the target classes chosen by the attacker [13, 76]. The challenge is that the channel may distort the injected image (in terms of color, brightness, and noise). Thus, we extend our projector-camera channel model with auto exposure control and color calibration, and we integrate the channel model into our optimization formulation, so that the optimizer is able to find those patterns that are able to fool the classifier, and resistant to channel effects at the same time. With these improvements, our attacks accomplished twice higher success rates.

Our contributions are summarized as follows.

- We are the first to study perception domain attacks against vision-based object classification systems, in which the attacker spoofs the image classifier by remotely injecting light carrying adversarially generated patterns into the camera, thus changing its perception.
- Our proposed GhostImage attacks are the first to leverage lens flare effects and exposure control. We propose a basic camera-aware attack that directly projects the adversarial image into the ghost area, and uses downsampling to adjust to different ghost resolutions.
- To improve the robustness of the attack, we integrate adversarial machine learning based optimization methods into GhostImage attacks to find optimal attack patterns that can spoof the image classifier with high confidence. We also propose and empirically validate an end-to-end projector-camera channel model that predicts the resolution and pixel location of of ghosts, as well as channel effects such as exposure control and color calibration. We incorporate the channel model into the optimization formulation so that the attack patterns are resistant to channel effects.
- We conduct comprehensive experiments to evaluate GhostImage attacks in terms of attack effectiveness and robustness. Results show that GhostImage attacks were able to achieve attack success rates as high as 100%, depending on the projector-camera distance.

2 SYSTEM, ATTACK AND THREAT MODEL

In this section we will setup our system model, and our attack model about two attack objectives, and threat model about the capabilities of two types of attackers.

2.1 System Model

We assume an end-to-end vision-based object classification system (Fig. 2) in which a camera captures an image of a scene with objects of interest. The image is then fed to an object detector to crop out the areas of objects, and finally these areas are given to a neural network to classify the objects. In autonomous systems, for example, the classification results will be used to make decisions and later actions will be taken accordingly. If any step makes mistakes, incorrect actions could be performed. For example, in autonomous driving scenario, if a STOP sign is misclassified as a YIELD sign, the vehicle will keep moving instead of stopping, which may result in traffic accidents.

2.2 Attack Objectives

In this paper, we consider two different attack objectives. The first one is called **creation attacks**, where the goal is to inject the image of an object into the camera, even though such an object does not physically exist in the scene. Moreover, the attacker aims to cause incorrect classification results to be made by a camera-based object classification system. In autonomous systems, for example, the attacker may inject an image of a STOP sign into a camera on an autonomous vehicle running on the highway to cause it stop on the highway.

The attacker can also mount **obfuscation attacks**, where there is already an object of interest in the scene, and the attacker injects some adversarial patterns that overlap with the original image of the object, so that the resulting image gets misclassified. For example, an attacker can inject patterns to obfuscate a STOP sign’s image in the camera so that an autonomous vehicle runs pass the STOP sign, since the classification system is fooled to believe that it is a YIELD sign instead.

2.3 Threat Model

We consider two types of attackers with differing capabilities:

Camera-aware attackers who possess knowledge of the victim’s camera (i.e., they do not know the configuration of the lens system, nor post-processing algorithms, but they can possess the same type of camera used in the target system), from which they can train a channel model using the camera as a black-box. With such capabilities, they are able to achieve creation attacks and obfuscation attacks.

System-aware attackers possess not only the capabilities of the camera-aware attackers, but also knows about the image classifier including its architecture and parameters, i.e., black-box attack on the camera but white-box attack on the classifier. With such capabilities, it is able to achieve creation attacks and obfuscation attacks as well, but with higher attack success rates.

Note that both types of attackers are remote, i.e., they do not have access to the hardware or the firmware of the victim camera, nor to the images that the camera captures.

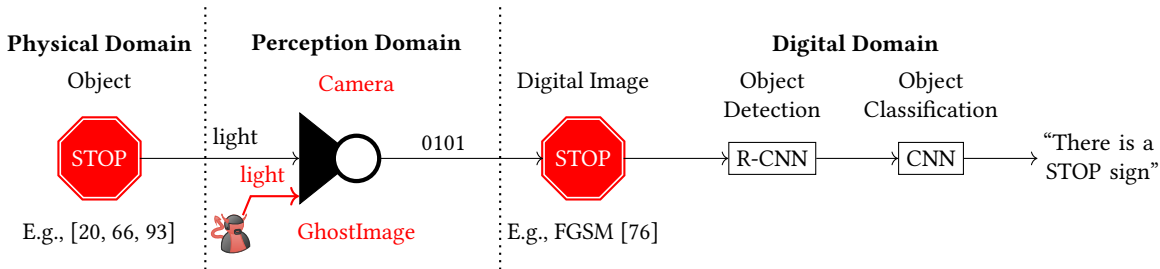


Figure 2: Vision-based object classification systems. GhostImage attacks target the perception domain, i.e., the camera.

3 BACKGROUND

In this section, we will introduce optical imaging principles, including flare/ghost effects and exposure control, which we will exploit to *realize* GhostImage attacks. Then, we will discuss the preliminaries about neural networks and adversarial examples that we will use to *enhance* GhostImage attacks.

3.1 Optical Imaging Principles

Due to the optical principles of camera-based imaging systems, it is not feasible to directly point a projector at a camera, hoping that the projected patterns can appear at the same location with the image of the targeted object, because the projector has to obscure the object in order to make the two images overlap. We prove this infeasibility in Appendix D. Instead, we exploit lens flare effects and auto exposure control to inject adversarial patterns.

Lens flare effects [26] refer to a phenomenon where one or more undesirable artifacts appear on an image because bright light get scattered or flared in a non-ideal lens system (Fig. 3). Ideally, all light beams should pass directly through the lens and reach the CMOS sensor. However, due to the quality of the lens elements, a small portion of light gets reflected several times within the lens system and then reaches the sensor, forming multiple polygons (called “ghosts”) on the image. The shape of polygons depends on the shape of the iris aperture. For example, if the aperture has six sides, there will be hexagon-shaped ghosts in the image. Normally ghosts are very weak and one cannot see them, but when a strong light source (such as the sun, a light bulb, a laser, or a projector) is present, the ghost effects become visible. Fig. 3 shows only one reflection path, but there are many other paths and that is why there are usually multiple ghosts in an image.

Existing literature [26, 33, 73] about ghosts focused on the simulation of ghosts given the detailed lens configurations, in which the algorithms simulate every possible reflection path. Such white-box models are computationally intensive, and requires white-box knowledge of internal lens configurations, thus are not suitable for

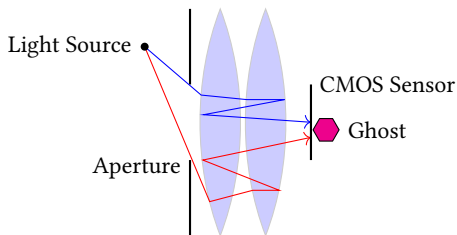


Figure 3: Ghost effect principle

our purposes. In Sections 4 and 5, we study flare effects in a black-box manner, where we train a lightweight end-to-end model that is able to predict the locations of ghosts, estimate the resolutions within ghost areas, and also calibrate colors.

Exposure control mechanisms [17, 32] are often equipped in cameras. In dark environments, the camera would increase its exposure so that the images would not look too dark; on the other hand, exposure would be decreased in bright environments, so that more details can be captured. There are two ways to control the exposure: A camera can adjust its size of the aperture, or the exposure time: the bigger/longer the aperture/exposure time is, the brighter the image will be. In this work, we will model and exploit auto exposure control to manipulate the brightness balance between the targeted object and the injected attack patterns in ghosts.

3.2 Neural Networks and Adversarial Examples

We abstract a neural network as a function $Y = f_{\theta}(x)$ and we omit the details of it due to the page limit. The input $x \in \mathbb{R}^{w \times h \times 3}$ (width, height and RGB channels) is an image, $Y \in \mathbb{R}^m$ is the output vector, and θ is the parameters of the network (which is fixed thus we omit it for convenience). A softmax layer is usually added to the end of a neural network to make sure that $\sum_{i=1}^m Y_i = 1$ and $Y_i \in [0, 1]$. The classification result is $C(x) = \text{argmax}_i Y_i$. Also, the inputs to the softmax layer are called *logits* and denoted as $Z(x)$.

An adversarial example [76] is denoted as y , where $y = x + \Delta$. Here, Δ is additive noise that has the same dimensionality with x . Given a benign image x and a target label t , an adversary wants to find a Δ such that $C(x + \Delta) = t$, i.e., *targeted attacks*. Note that, in this paper, the magnitude of Δ is not constrained below a small threshold, since the perceived images are usually not directly observed by human users. But we still try to minimize it because it represents the attack power and cost.

4 CAMERA-AWARE GHOSTIMAGE ATTACKS

In this section, we will discuss how a camera-aware attacker is able to inject arbitrary patterns in the perceived image of the victim camera using projectors. We will discuss the possibilities of using other attack vectors in Section 7.2.

4.1 Technical Challenges

Since we assume that we do not have access to the images that the targeted camera captures, the attacker will have to be able to predict how ghosts might appear in the image. First, the locations of ghosts should be predicted given the relevant positions of the projector and the camera, so that the attacker can align the ghost with the image

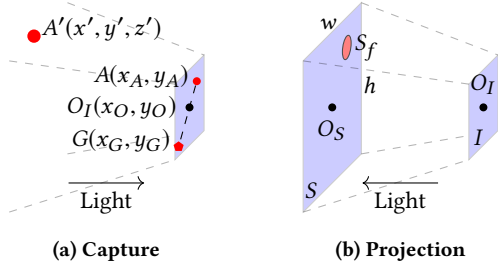


Figure 4: Capture and projection are reverses of each other.

of the object of interest to achieve obfuscation attacks. Second, since a projector can inject shapes in ghost areas, the attacker needs to find out the maximum resolution of shapes that it can inject. Lastly, it is also challenging to realize the attacks derived from the position and resolution models above with a limited budget.

4.2 Ghost Pixel Coordinates

Given the pixel coordinates of the target object G (Fig. 4a), we need to derive the real-world coordinates A' of the projector so that we know where to place the projector in order to make the ghost overlap with the image of the object. To do this, we derive the relationship between G and A' in two steps: We first calculate the pixel coordinates of the light source A given A' , and then we calculate G based on A .

Based on homogeneous coordinates [77], assuming the camera is at the origin of the coordinate system, A can be derived as

$$(u, v, w)^T = M \cdot (x', y', z', 1)^T, \quad (1)$$

where M is the camera's geometric model [77], a 3×4 matrix. M can be trained from another (similar) camera, and then be applied to the victim camera. The coordinates of A is then $A = (x_A, y_A)^T = (u/w, v/w)^T$, by the homogeneous transformation.

In order to find the relationship of the pixel coordinates between light sources A and their ghosts G , we did a simple experiment where we moved around a flashlight in front of the camera [51], and recorded the pixel coordinates of the flashlight and the biggest ghost. We observe that $\overline{AO_I}/\overline{O_I G} = r$, for all pairs of A and G (Fig. 13 in Appendix B), and the ratio r is roughly 0.4 based on our setup. Finally, given $A = (x_A, y_A)$, $O_I = (x_O, y_O)$ and r ,

$$G = \begin{pmatrix} x_O - (x_A - x_O)/r \\ y_O - (y_A - y_O)/r \end{pmatrix}. \quad (2)$$

With G 's coordinates, the attacker is able to predict where the ghost would appear in the image and try adjusting the location of the light source in the real world so as to align the ghost with the image of the object, whose pixel coordinates can be calculated using Eq. (1) similarly.

4.3 Ghost Resolutions

In our daily life, ghosts normally appear as pieces of single-color polygon-shaped artifacts; this is because the light sources that cause these regular ghosts are single-point sources of light that have just one single color, such as light bulbs, flashlights, etc. In this work, however, we find out that one is able to bring patterns into these ghost areas, by simply using a regular classroom-use projector, a special source of light that shines variant patterns in variant colors.

For example, in Fig. 1, an image of a STOP sign that is projected by a projector, appears in one of the ghost areas in the image; this is because the pixel resolution of the projector is high enough that multiple light beams in different colors (got reflected among lenses and then) go into the same ghost. In this subsection, we study the resolution of the patterns in ghost areas¹.

Let us first define the *throwing ratio* of a projector. In Fig. 4b, let plane S be the projected screen (e.g. on a wall), whose height and width are denoted as h and w , respectively. The distance $d = \overline{O_S O_I}$ is called the throwing distance. The throwing ratio of this projection is $r_{\text{throw}} = d/w$. The (physical) size of the projected screen at the victim camera's location is denoted S_O , part of which is captured by the CMOS sensor of the camera in the ghost area, and we denote the (physical) size of that area as S_f . Let us also define the resolution of the entire projected screen as P_O in terms of pixels (e.g., 1024×768), and the resolution of the ghost as P_f . Clearly, there is a linear relationship among them: $P_f/P_O = S_f/S_O$, where $S_O = wh$. Finally, we can calculate the resolution of the ghost given d and r_{throw} :

$$P_f = \frac{P_O S_f}{\frac{h}{w} \left(\frac{d}{r_{\text{throw}}} \right)^2}. \quad (3)$$

Here, S_f is a constant because the size of the lens is fixed. We can obtain S_f by deriving from Eq. (3) only once for one camera. Take the camera [51] for an example, its S_f is 0.0156 cm^2 .

4.4 Attack Realization and Experiment Setup

According to Eq. 3, if the attacker wants to carry out long-distance and high-resolution GhostImage attacks, it needs a projector with a large throwing ratio r_{throw} . However, the factory longest-throw lenses (NEC NP05ZL Zoom Lens [49]) of our projector have some limitations. First of all, the maximum throwing ratio is only 7.2, which is only able to achieve 9×9 -resolution attacks at a distance of one meter. Second, they are expensive (about \$1,600), and they were discontinued by the manufacturer.

Rather than a factory lens, we use a cheap (\$80) zoom lens (Fig. 5) [9] that was originally designed for Canon cameras. Since projectors and cameras are dual devices (Fig. 4), their lenses are theoretically exchangeable. In our experiments, the Canon zoom lens is indeed practically suitable for our NEC projector [47] (Fig. 5), achieving the maximum throwing ratio of 20 when the focal length is 250 mm, which means that at a distance of one meter, 32×32 -resolution attacks can be achieved. Note that there are other telephoto zoom lenses with much longer focal lengths, e.g., for \$200, one can acquire an Opteka telephoto zoom lens [53] that supports up to 1300 mm, which means a throwing ratio of roughly 100 and the max resolution of 160×160 at one meter.

Fig. 5 (left) shows a general diagram of GhostImage attacks, where the light source (i.e., a projector) is pointing at the camera from the side, so that the camera can still capture the object (e.g., a STOP sign) for obfuscation attacks. The light source injects some light interference (marked in blue) into the camera, which gets reflected among the lenses of the camera, resulting in ghosts that overlap with the object in the image. Accordingly, a photo of our

¹We are interested in the resolution of the projector pixels, not camera pixels; a projector pixel is usually captured by multiple camera pixels.



Figure 5: (Left) Attack setup diagram. (Middle) In-lab experiment setup. (Right) Attack equipments: We replaced the original lens of the NEC NP3150 Projector [47] with a Canon EFS 55-250 mm zoom lens [9].

in-lab experiment setup is given in Fig. 5. The Canon Lens was loaded in the NEC projector, though it cannot be seen in the photo. We used an Aptina MT9M034 camera [51] as the targeted camera since it was designed for autonomous driving. We will evaluate other cameras in Section 6.2.3.

To mount a creation attack, the attacker computes the maximum resolution P_f for the ghost with a distance d based on Eq. (3), and then *downsamples* the target image to the resolution P_f in order to fit in the ghost area. The attacker chooses downsampling as a heuristic approach because he/she is not aware of the classification algorithm. In Appendix E, we present in Fig. 16 some examples of downsampling a STOP sign image.

To mount obfuscation attacks, in addition to Eq. (3) for downsampling, the attacker also needs to consider the pixel coordinates (Eq. (2)) of the ghost because the attacker needs to align the ghost with the image of the object of interest so that the resulting combined image fools the classifier.

4.5 Experimental Results

4.5.1 Dataset and neural network architecture. We use the LISA dataset [44], which consists of images of traffic signs in the United States. In order to train an unbiased classifier, we selected eight traffic signs (Table 6 in Appendix A). The network architecture (Table 5 in Appendix A) is identical to [20]. We used 80% of samples from the balanced dataset to train the network and the rest 20% to test the network; it achieved an accuracy of 96%.

4.5.2 Evaluation methodology. The evaluation procedure for obfuscation attacks is detailed in Algorithm 1 in Appendix E, in which we iterated five distances, m source classes, m target classes. For each target class, we sampled k images randomly from the LISA dataset. For every combination, we first downsampled the target image based on Eq. (3), and projected the image at the camera using the NEC projector. We then took the captured image, cropped out the ghost area, and used the classifier to classify it. If the classification result is the target class, we count it as a successful attack. The procedure for creation attacks is slightly different: rather than placing printed traffic signs, we use a blackboard as the background because it helped us locate the ghost.

Given that the Canon lens helps us achieve the max throwing ratio of 20, we evaluated five different distances from one meter to five meters. Based on Eq. (3), they resulted in 32×32 , 16×16 , 8×8 , 4×4 , and 2×2 resolutions, respectively.

4.5.3 Results. The results about attack success rates of camera-aware attacks at varying distances are shown in Table 1 (Fig. 6 illustrates two successful camera-aware attacks). For the digital domain, we simply added attack images Δ on benign images x as

$y = (x + \Delta) / \|x + \Delta\|_\infty$. Based on these experiments, we observe: First, as the distance increases, the success rate decreases. This is because lower-resolution images are less well recognized by the classifier. Second, digital domain results are better than perception domain one, because images are distorted by the projector-camera channel effects. We will discuss how to resolve such channel effects in Section 5. Third, creation attacks result in higher success rates than obfuscation attacks do because in obfuscation attacks there are benign images in the background, encouraging the classifier to make correct classifications.

5 SYSTEM-AWARE GHOSTIMAGE ATTACKS

There are some limitations of the camera-aware attack introduced in the previous section. First, increasing distances results in lower success rates because the classifier cannot recognize the resulting low-resolution images. Second, there are large gaps between digital domain results and perception domain results, as channel effects (which cause the inconsistency between the intended pixels and the perceived pixels) are not taken into account. In this section, we resolve these limitations and improve GhostImage attacks' success rates by proposing a framework which consists of a channel model that predicts the pixels perceived by the camera, given the pixels as input to the projector, as well as an optimization formulation based

Table 1: Camera-aware attack success rates

Distances (meter)	Creation Attacks		Obfuscation Attacks	
	Digital	Perception	Digital	Perception
1	98%	41%	95%	33%
2	98%	36%	88%	33%
3	80%	34%	67%	34%
4	36%	15%	28%	10%
5	14%	10%	13%	0%



Figure 6: Camera-aware attack examples at one meter in perception domain. Left: Creating a Merge sign. Right: Obfuscating a STOP sign (in the background) into a Merge sign.

on which the attacker can solve for optimal attack patterns that cause misclassification by the target classifier with high confidence.

5.1 Technical Challenges

First, the injected pixel values are often difficult to control as they exhibit randomness due to variability of the channel between the projector and the camera, thus the adversary is not able to manipulate each pixel deterministically. Second, to achieve optimal results, the attacker needs to precisely predict the projected and perceived pixels, thus channel effects must be modeled in an end-to-end manner, i.e., considering not only physical channel (air propagation), but also the projector and the camera’s internal processes. Lastly, the resolution of attack patterns is limited by distances and projector lens (Eq. 3), thus optimal ghost patterns must be carefully designed to fit the resolution with few degrees of freedom.

5.2 System-aware Attack Overview

The system-aware attacker aims to find optimal patterns that can cause misclassification by the target classifier with high confidence by taking advantage of the non-robustness of the classifier [76]. We adopt an adversarial example-based optimization formulation into GhostImage attacks, in which the attacker tries to solve

$$\Delta^* = \arg \min_{\Delta} \|\Delta\|_p + c \cdot \mathcal{L}_{\text{adv}}(y, t, \theta), \quad (4)$$

where Δ is the digital attack pattern as input to the projector, x is the benign image of the object of interest, t is the target class, and θ represents the targeted neural network but we will omit it for convenience. $\|\cdot\|_p$ is an p -norm that measures the magnitude of a vector, and \mathcal{L}_{adv} is a loss function indicating how (un)successful Δ is. Here we aim to minimize projector’s power needed for a successful attack, and maximizing the successful chance of attacks. The relative importance of these two objectives is balanced by a constant c . More importantly, y is the final perceived image used as input to the classifier, which is estimated by our channel model:

$$y = g\left(h_f(\Delta) + h_o(x)\right), \quad (5)$$

where $h_f(\Delta)$ is the ghost model that estimates the perceived adversarial pixel values in the ghost. For simplicity we let $h_o(x) = x$ because the attacker possesses same type of the camera so that x can be obtained a priori, and $g(\cdot)$ is the auto exposure control that adjusts the brightness. Next, we will first present the channel model, and then formulate the optimization problem for finding optimal adversarial ghost patterns.

5.3 Projector-Camera Channel Model

We consider the projector to camera channel model (Fig. 7) in which δ^2 is an RGB value the attacker wishes to project which is later converted to an analog color by the projector. The attacker can control the power (P_a) of the light source of the projector so that the luminescence can be adjusted. The targeted camera is situated at a distance of d , which captures the light coming from both the projector and reflected off the object (x). The illuminance received by the camera from the projector is denoted as \mathcal{I} . The camera

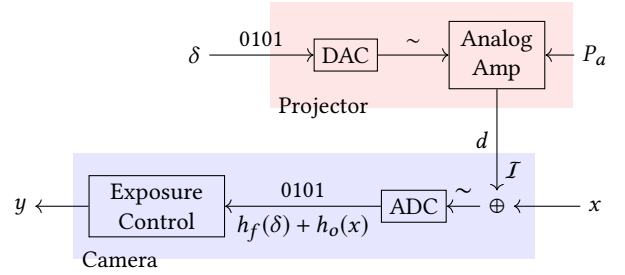


Figure 7: Projector-camera channel model

converts analog signals into digital ones, based on which it adjusts its exposure, with the final RGB value being y . An ideal channel would yield $y = x + \delta$ but due to channel effects, we need to find a way to adjust the projected RGB value such that the perceived RGB value is as intended.

5.3.1 Exposure control. As we discussed in Section 3.1, cameras are usually equipped with auto-exposure control, where according to the overall brightness of the image, the camera adjusts its exposure by changing the exposure time, or the size of its aperture, or both. We observed from our experiments that, as we increase the luminescence of the projector (\mathcal{I}), in the image the brightness of the object (x) decreases but the ghost (δ) does not decrease as much. Modeling such phenomena helps the attacker to precisely predict the perceived image. We first find out how the illuminance \mathcal{I} depends on δ and P_a (the normalized power of light bulb ranging from 0% to 100%), and then how y depends on \mathcal{I} .

How does \mathcal{I} depend on δ and P_a ? We conducted a series of experiments, where $T_d = \|\delta\|_{\infty} = \max_i \delta_i$ and P_a were varied. We recorded the illuminance directly in front of the camera using an illuminance meter [41], with the projector one meter away. The results are plotted in Fig. 14 in Appendix B, which shows that

$$\mathcal{I}(T_d, P_a, d) = \frac{c_d}{d^2} \cdot \frac{\mathcal{I}_{\text{max}}}{1 + e^{-t}}, \quad (6)$$

where $t = a \times T_d + b \times P_a + c_t$, and a, b, c_d and c_t are constants derived from the data. \mathcal{I}_{max} is the maximum illuminance of the projector at a distance of one meter. Such a sigmoid-like function captures the luminescence saturation property of the projector’s hardware.

How does the perceived x depend on \mathcal{I} ? In the same experiments we also recorded the RGB value of the ghost (δ) with a blackboard as background (in order to reduce ambient impacts), and a piece of white paper (x) that was also on the blackboard but did not overlay with the ghost. Their data are shown in Fig. 15 in Appendix B, from which we can derive the *dimming ratio* that measures the change of exposure/brightness:

$$\gamma(\mathcal{I}) = \frac{\mathcal{I}_{\text{env}}}{\mathcal{I} + \mathcal{I}_{\text{env}}}, \quad (7)$$

where \mathcal{I}_{env} is the ambient lighting condition in illuminance which differs from indoors to outdoors for instances. From this equation, we see that in an environment with static lighting condition, as the luminescence of the projector increases, the dimming ratio decreases, hence the objects become darker.

How does the perceived δ depend on \mathcal{I} ? When $x = 0$, $\|y_f\| = \|y_f\|_{\infty}$ (the lower subplot of Fig. 15 in Appendix B) depends on \mathcal{I}

²Different than Δ which is a $w \times h \times 3$ sensor, δ is a single pixel with dimension 3×1 for the convenience of the analysis.

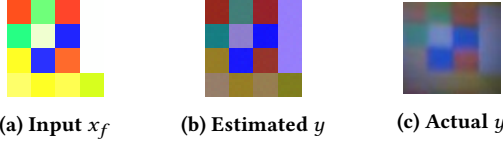


Figure 8: An example of channel model prediction

in two ways: $\|y_f\|(I) = \gamma(I) \cdot \rho \cdot I$. On one hand, the last term I increases the intensity of ghosts, but on the other hand the dimming ratio $\gamma(I)$ dims down ghost, and ρ is a trainable constant. With this, we can rewrite the perceived flare as $y_f = \|y_f\|H_c\delta/\|\delta\|$, where H_c is the color calibration matrix to deal with color distortion, which will be discussed in Section 5.3.2. The term $1/\|\delta\|$ normalizes δ . In the end, we have the channel model

$$y = \gamma(I) \left(\rho I H_c \frac{\delta}{\|\delta\|} + x \right). \quad (8)$$

Compared with Eq. (5), $h_f(\delta) = \rho I H_c \delta / \|\delta\|$, and $g(t) = \gamma(I)t$. With Eq. (8), the attacker is able to predict how bright and what colors/pixel values the ghost and the object will be, given the projected pixels, projector’s power and the projector-camera distance.

5.3.2 Color calibration. Considering a dark background (i.e., $x = 0$), Eq. (8) can be simplified as $y = \gamma(I)\rho I H_c \delta / \|\delta\|$, where H_c is a 3×3 matrix (as three color channels) that calibrates colors. Both y and δ are 3×1 column vectors. H_c should be an identity matrix for an ideal channel, but due to the color-imperfection of both the projector and the camera, H_c needs to be learned from data. To simplify notations, we define corrected x and y , respectively as $\hat{x} = \delta / \|\delta\|$, and $\hat{y} = y / [\rho I \gamma(I)]$, so that we can write $\hat{y} = H_c \hat{x}$.

We did another set of experiments where we collected $n = 100$ pairs of (\hat{x}, \hat{y}) with dark background (to make $x = 0$), with δ being assigned randomly, and $P_a = 30\%$. We grouped them into X and Y : $X = [\hat{x}_1^\top, \hat{x}_2^\top, \dots, \hat{x}_n^\top]^\top$, and $Y = [\hat{y}_1^\top, \hat{y}_2^\top, \dots, \hat{y}_n^\top]^\top$, where both X and Y are $n \times 3$ matrices. We compute H_c by solving

$$\min_{H_c} \|Y - XH_c\|_2^2.$$

This is known as a non-homogeneous least square problem [77], and it has a closed-form solution: $H_c = ((X^\top X)^{-1} X^\top Y)^\top$.

5.3.3 Model validation. Fig. 8 demonstrates the accuracy of our channel model. In it the left image is the original input to the projector, the middle image is the estimated output from the camera based on our channel model (Eq. (8)), and the image on the right is the actual image in a ghost captured by the camera. As can be seen, the difference between the actual and predicted is much less than the actual and original. While blurring effect is apparent in the actual y , we do not model it but the success rates are still high despite it. As we will see in Section 6, our channel model is general enough that once trained on one camera in one environment, it can be transferred to different environments and different cameras without retraining.

5.4 Optimal Adversarial Projection Patterns

In long-distance, low-resolution GhostImage attacks there are only a few pixels in the ghost area. A camera-aware attacker’s strategy is to simply downsample attack images into low resolutions, but that does not result in high success rates. While Eq. (4) is abstract,

for the rest of this subsection, we will progressively detail it and show how it can be solved in light of the channel model to improve attack success rates. We will start with the simplest situation of single-color ghosts in order to explain how we handle random noise (Sec. 5.1). Later, we will consider how to find semi-positive additive noise due to the fact that superposition can only increase perceived light intensity but not decrease it. Third, we examine the optimization problem to find optimal ghost patterns in grids at different resolutions.

5.4.1 Single-color ghost. Let us consider the simplest case first where the random noise Δ is drawn from one single Gaussian distribution for all three channels, i.e., $\Delta \sim \mathcal{N}(\mu, \sigma^2)$, where the size of Δ is $w \times h \times 3$ and w and h represent the width and height of the benign image x . This is because the values of each pixel that appear in the ghost area follow Gaussian distributions according to statistics obtained from our experiments. The adversary needs to find μ and σ such that when Δ is added to the benign image x , the resulting image y will be classified as the target class t . That said, the logits value (Section 3.2) of the target class should be as high as possible compared with the logits values of other classes [13]. Such a difference is measured by the loss function $\mathcal{L}_{\text{adv}}(y, t)$

$$\mathcal{L}_{\text{adv}}(y, t) = \max \left\{ -\kappa, \max_{i:i \neq t} \{\mathbb{E}[Z_i(y)]\} - \mathbb{E}[Z_t(y)] \right\}, \quad (9)$$

where $\mathbb{E}[Z_i(y)]$ is the expectation of logits values at class i of input y . Term $\max_{i:i \neq t} \{\mathbb{E}[Z_i(y)]\}$ is the highest expected logits value among all the classes except the target class t , and $\mathbb{E}[Z_t(y)]$ is the expected logits value of t . Here, κ controls the logits gap between $\max_{i:i \neq t} \{\mathbb{E}[Z_i(y)]\}$ and $\mathbb{E}[Z_t(y)]$; the larger the κ is, the more confident that Δ is successful. The attacker needs \mathcal{L}_{adv} as low as possible so that the neural network would classify y as class t . Most importantly, y is computed based on our channel model (Eq. (8)), so that the optimizer finds the optimal ghost patterns that are resistant to the channel effects. Unfortunately, due to the complexity of neural networks, the expectations of logits values $\mathbb{E}[Z_i(y)]$ are hard to be expressed analytically; we instead use Monte Carlo methods to approximate it:

$$\hat{\mathbb{E}}[Z_i(y)] = \frac{1}{T} \sum_{j=1}^T Z_i(y_j), \quad (10)$$

where T is the number of trials, and y_j is for the j -th trial.

Meanwhile, the adversary also needs to minimize the magnitude of Δ to reduce the attack power and noticeability, as well as its peak energy consumption (as the larger σ is, the higher the power peak could be). With Δ being a random vector, we compute the expectation of its magnitude:

$$\mathbb{E}[\|\Delta\|_p] = \mu n^{1/p}. \quad (11)$$

Putting (9) and (11) together with a tunable constant c , we have our optimization problem for the simplest case

$$\begin{aligned} \mu^*, \sigma^* &= \arg \min_{\mu, \sigma} \quad \mathbb{E}[\|\Delta\|_p] + \sigma + c \cdot \mathcal{L}_{\text{adv}}(y, t), \\ &\text{subject to} \quad \sigma > \sigma_l, \end{aligned}$$

Here, σ_l is the lower bound of the standard deviation σ , meaning that the interference generator and the channel environment can provide random noise with at least the standard deviation of σ_l .

When $\sigma_I = 0$, the adversary is able to manipulate pixels deterministically. Therefore, when we fix σ as σ_I in the optimization problem, the attack success rate when deploying μ^* would be the lower bound of the attack success rate. In other words, the adversary equipped with an attack setup that can produce noise with lower variance can mount attacks with a higher success rate. Therefore we can simplify our formulation by removing the constraint about σ , and the optimization problem now becomes

$$\mu^* = \arg \min_{\mu} \mathbb{E}[\|\Delta\|_p] + c \cdot \mathcal{L}_{\text{adv}}(y, t). \quad (12)$$

For the rest of the paper we will simply use σ to denote σ_I .

Since in Eq. (12) there is only one variable that the adversary is able to control, it is infeasible to launch a targeted attack with such few degrees of freedom. As a result, the adversary needs to manipulate each channel individually. That is, for each channel, there will be an independent distribution from which noise will be drawn. This is feasible because noise can appear in different colors in the ghost areas in which three channels are perturbed differently when using projectors. Let us decompose Δ as $\Delta = [\Delta_R, \Delta_G, \Delta_B]$, where the dimension of $\Delta_{\{R,G,B\}}$ is $w \times h$, and they follow three independent Gaussian distributions

$$\Delta_R \sim \mathcal{N}(\mu_R, \sigma_R^2), \quad \Delta_G \sim \mathcal{N}(\mu_G, \sigma_G^2), \quad \Delta_B \sim \mathcal{N}(\mu_B, \sigma_B^2).$$

Here, $\mu_{\{R,G,B\}}$ and $\sigma_{\{R,G,B\}}$ are the means and the standard deviations (σ) of the three Gaussian distributions, respectively. The expectation of such Δ is then

$$\mathbb{E}[\|\Delta\|_p] = \left[\frac{n}{3} (\mu_R^p + \mu_G^p + \mu_B^p) \right]^{\frac{1}{p}}. \quad (13)$$

Eq. (11) is a special case of (13) when $\mu = \mu_R = \mu_G = \mu_B$. We denote $\boldsymbol{\mu} = [\mu_R, \mu_G, \mu_B]^T$. Hence, similar to (12), we have the optimization problem for single-color perturbation

$$\boldsymbol{\mu}^* = \arg \min_{\boldsymbol{\mu}} \mathbb{E}[\|\Delta\|_p] + c \cdot \mathcal{L}_{\text{adv}}(y, t), \quad (14)$$

by which the adversary finds the optimal $\boldsymbol{\mu}^*$ from which Δ is drawn.

5.4.2 Non-negative noise constraint. Eq. (14) must be solved with the constraint $\Delta \geq 0$ because the adversary can only increase the light. Rather than explicitly place a constraint in (14), we propose to punish negative values, by introducing *biased penalty*

$$R(\Delta) = e^{-\alpha(\Delta-\omega)} + e^{\beta(\Delta-\omega)} - \eta, \quad (15)$$

where

$$\omega = \frac{\ln \alpha - \ln \beta}{\alpha + \beta}, \quad \eta = \left(\frac{\alpha}{\beta} \right)^{\frac{-\alpha}{\alpha+\beta}} + \left(\frac{\alpha}{\beta} \right)^{\frac{\beta}{\alpha+\beta}}.$$

Here ω is to center the global minimum at Δ being zero, and subtracting η is to lower the minimum to be zero but it does not change the optimization results so we will omit it. An instance of (15) when $\alpha = 2$ and $\beta = 1$ is plotted in Fig. 17 in Appendix C in comparison with the L_2 norm. With the same absolute value, while the L_p norm treats positive perturbation and negative perturbation equally, the biased penalty function punishes the negative values more than the positive one, encouraging the optimization algorithm to find positive Δ . We adopt it into our optimization formulation

$$\boldsymbol{\mu}^* = \arg \min_{\boldsymbol{\mu}} \mathbb{E}[R(\Delta)] + c \cdot \mathcal{L}_{\text{adv}}(y, t), \quad (16)$$

and in the experiments we set $\alpha = 8$ and $\beta = 2$.

5.4.3 Ghost grids. Since projector's pixels are arranged in grids, the attack patterns are in grids as well, especially in lower resolutions. We enable Δ with patterns in different resolutions. Such a grid pattern Δ can be composed of several blocks $\Delta_{i,j,k}$, i.e., $\Delta_{i,j,k} : \{1 \leq i \leq N_{\text{row}}, 1 \leq j \leq N_{\text{col}}, 1 \leq k \leq N_{\text{chn}}\}$ where $N_{\text{row}}, N_{\text{col}}$ and N_{chn} is the number of rows, columns, and channels of a grid pattern, respectively, in terms of blocks. In a word, $\Delta_{i,j,k}$ is the perturbation block at i -th row, j -th column and k -th channel. A block $\Delta_{i,j,k}$ is a random matrix and its size is $\frac{w}{N_{\text{col}}} \times \frac{h}{N_{\text{row}}}$, so that the size of Δ is still $w \times h \times 3$. Besides, the elements in the random matrix $\Delta_{i,j,k}$ is i.i.d. drawn from a Gaussian distribution, i.e., $\Delta_{i,j,k} \sim \mathcal{N}(\mu_{i,j,k}, \sigma^2)$.

The adversary can find the optimal grid pattern Δ by solving the optimization problem as in Eq. (16) in which

$$\mathbb{E}[R(\Delta)] = \sum_{i=1}^{N_{\text{row}}} \sum_{j=1}^{N_{\text{col}}} \sum_{k=1}^{N_{\text{chn}}} e^{-\alpha(\mu_{i,j,k}-\omega)} + e^{\beta(\mu_{i,j,k}-\omega)}, \quad (17)$$

where $\mu_{i,j,k}$ is the mean of the block $\Delta_{i,j,k}$. See Fig. 18a in Appendix C for an illustration of the dimensionality of $\mu_{i,j,k}$, and Fig. 18b in Appendix C for the resulting pattern in color.

6 SYSTEM-AWARE ATTACK EVALUATIONS

In this section, we present the evaluation of the system-aware attacks in terms of *attack effectiveness*, namely how well system-aware attacks perform in the same setup as camera-aware attacks (Section 4.5), and *attack robustness*, namely how well system-aware attacks are when being evaluated in different setups. We will again use attack success rates (Algorithm 1) as our metric. We used the Adam Optimizer [27] to solve our optimization problems.

We present two sets of results: *Emulation results* refer to the classification results on emulated, combined images of benign images and attack patterns using our channel model (Equation 8). Emulation helps us conduct scalable and fast evaluations of GhostImage attacks before conducting real-world experiments. *Experimental results* refer to the classification results on the images that are actually captured by the victim cameras when the projector is on.

6.1 Attack Effectiveness

To compare with camera-aware attacks, system-aware attacks are evaluated in a similar procedure (Algorithm 1), targeting a camera-based object classification system with the LISA dataset and its classifier, and the Aptina MT9M034 camera [51], in an in-lab environment. The main difference is that the attack patterns are found by our optimization framework rather than downsampling.

6.1.1 Creation attacks. For emulated creation attacks, all distances (or all resolutions) yielded attack success rates of 100% (Fig. 9), which means that our optimization problem were easy to solve. In terms of computational overhead, we need roughly 30 seconds per image at 2×2 -resolution, and 10 seconds at 4×4 or above (because of larger degrees of freedom) using NVIDIA Tesla P100 [50]. Fig. 10a shows examples of emulated attack patterns for creation attacks, along with the images of real signs on the top. Interestingly, high-resolution shapes do look like real signs. For example, we can see three vertical bars for ADDEDLANE, and also we can see a circle at

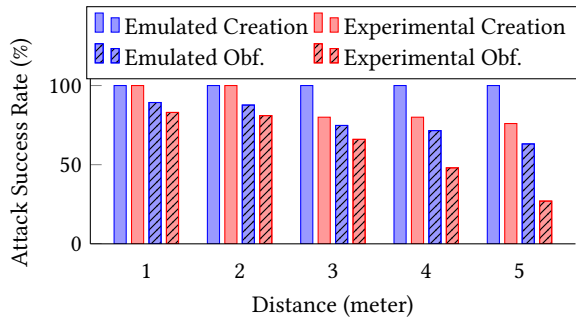


Figure 9: System-aware creation and obfuscation (obf.)

the middle south for STOPAHEAD, etc. These results are consistent with the ones from the MNIST dataset [56] where we could also roughly observe the shapes of digits. Secondly, they are blue tinted because our channel model indicated that ghosts tended to be blue, thus the optimizer was trying to find “blue” attack patterns that could fool the classifier.

Thirdly, when we were solving an optimization problem targeting one class from k different (random) starting points, all k resulting attack patterns looked similar to the ones shown in Fig. 10a. However, results from datasets CIFAR-10 [29] and ImageNet [18] are much different: those patterns look rather random compared to the results from LISA or MNIST. The reason might be that in CIFAR-10, images in the same category are still very different, such as two different cats, but in LISA, two images of STOP signs do not look as different as two cats.

For the experimental results of creation attacks, we see that as distances increase, success rates decrease a little (Fig. 9), but are still four times higher than the camera-aware attacks (Table 1), because the optimization formulation helped find those optimal attack patterns with high confidence.

6.1.2 Obfuscation attacks. The emulation and experimental results of obfuscation attacks are shown in Fig. 9. Compared with creation attacks, obfuscation attacks perform a bit worse, especially for large distances (three meters or further). This is because the classifier also “saw” the benign image in the background and tends to classify the entire image as the benign class. Moreover, the alignment of attack patterns and the benign signs is imperfect, hence lower rates. However, when we compare Fig. 9 with Table 1 for camera-aware obfuscation attacks, we can still see 300% improvements. Fig. 10b provides an example of system-aware obfuscation attacks in the perception domain, which were trying to obfuscate the (printed) STOP sign into other signs: they look “blue” as the channel model predicted. The fifth column is not showing as it is STOP.

A misclassification matrix of emulated obfuscation attacks at 8×8 attack resolution is given in Table 2. The overall attack success rate was 75%. Each cell denotes the success rate of obfuscating a benign class (actual) into a target class (predicted). Most of them are 100%, but the SCHOOL sign, for example, was the most difficult to perturb *into* (the 3rd column) and yet not that hard to perturb *from* (the 3rd row), probably because it is in green (RGB: 0-255-0) and in an opened-envelope shape, while all the others are either red (255-0-0) or yellow (255-255-0) colors, and either polygon or rectangle shapes.

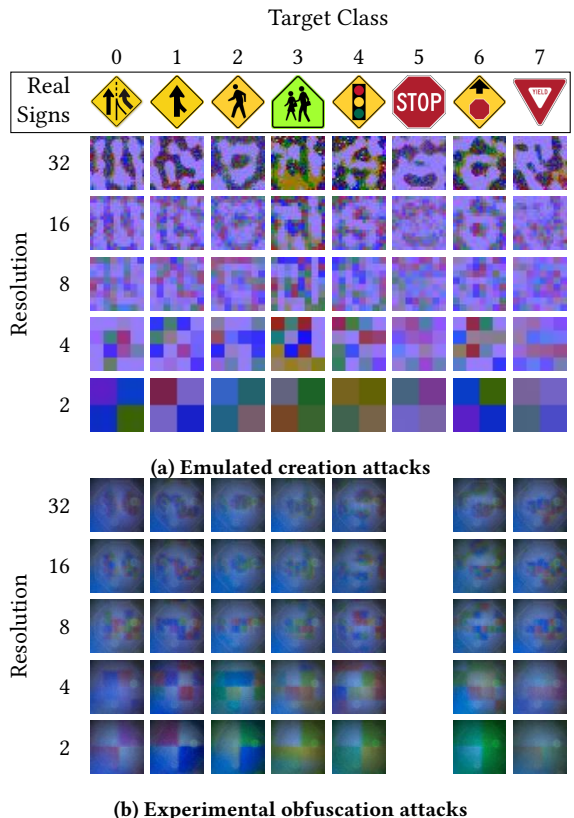


Figure 10: System-aware attack pattern examples.

6.2 Attack Robustness

Previously, our attacks were evaluated using the LISA traffic sign dataset, in an in-lab environment, using the Aptina MT9M034 camera [51]. In this section, we evaluate the robustness of our attacks in terms of different datasets, under different environments, and different cameras.

6.2.1 Different datasets. Here we evaluate our system-aware attacks on two other datasets, CIFAR-10 [29] and ImageNet [18], by emulation only because previous results showed that our emulation methods yielded similar success rates as experimental results.

CIFAR-10: The network architecture and model hyper parameters are shown in Table 7 and Table 8 in Appendix A, which are

Table 2: Emulated system-aware obfuscation attacks: misclassification matrix at 8×8 -resolution.

		Predicted							
		0	1	2	3	4	5	6	7
Actual	0	100	0	100	100	100	100	0	100
	1	0	100	100	0	100	100	100	100
	2	0	100	100	0	100	100	100	100
	3	100	0	100	100	100	100	0	97.2
	4	0	100	100	0	100	100	100	100
	5	100	100	90	0	100	100	100	100
	6	100	100	100	100	100	100	100	100
	7	100	100	0	0	0	100	100	100

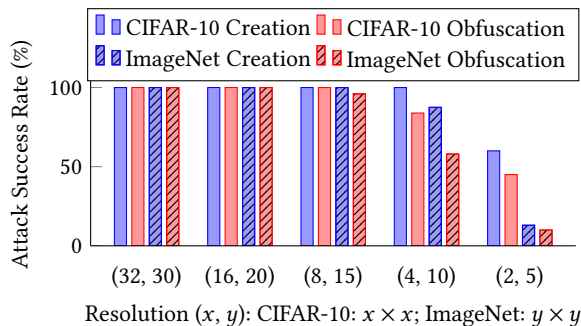


Figure 11: Emulated system-aware attacks on CIFAR-10 and ImageNet

identical to [13]. The network was trained with the distillation defense [57] so that we can evaluate the robustness of our attacks in terms of adversarial defenses. A classification accuracy of 80% was achieved. The evaluation procedure is similar to Algorithm 1.

Results are shown in Fig. 11. The overall trend is similar to the LISA dataset, but the success rates are significantly higher. The reason might still be the large variation within one class (Section 6.1.1), so that the CIFAR-10 classifier is not as sure about one class as the LISA classifier is, hence more vulnerable to GhostImage attacks.

ImageNet: We used a pre-trained Inception V3 neural network [75] for the ImageNet dataset to evaluate the attack robustness against large networks. Since the pre-trained network can recognize 1000 classes, we did not iterate all of them (similar to [13]). Instead, for obfuscation attacks, we randomly picked ten benign images from the validation set, and twenty random target classes, while for creation attacks, the “benign” images were purely black.

Results are given in Fig. 11. For high resolutions ($\geq 15 \times 15$), the attack success rates were nearly 100%. But as soon as the resolutions went down to 10×10 or below, the rates decreased sharply. The reason might be that in order to mount successful *targeted* attacks on a 1000-class image classifier, a large number of degrees of freedom are required. With 10×10 or lower resolution as well as three color channels might not be enough to accomplish targeted attacks. To verify this, we also evaluated untargeted obfuscation attacks on ImageNet (by default, GhostImage attacks are targeted attacks). Results show that when the resolutions were 1×1 or 2×2 , the success rates were around 50% or 80%, respectively. But as soon as the resolutions went to 3×3 or above, the success rates reached 100%. Lastly, similar to CIFAR-10, system-aware attacks on ImageNet were more successful than on LISA, because of high variation within one class.

Remark: Results from both datasets demonstrate that the system-aware GhostImage attack can be applied to varying datasets, where the channel model remains the same. Note that our attacks do not require a small norm bound on the noise magnitude (unlike physical or digital domain attacks). Thus the dataset/network architecture has less impact on the robustness.

6.2.2 On-road (outdoor) experiments. In order to evaluate system-aware attacks in a real-world environment, we also conducted experiments on-site (Fig. 12), where the camera was put on the hood of a vehicle that was about to pass an intersection with a STOP sign. The attacker’s projector was placed on the right curb, and it

Table 3: On-road obfuscation attack success rates

Success rates of	Noon	Dusk	Night
Overall	0%	51%	42.9%
STOP \rightarrow YIELD	0%	100%	100%
STOP \rightarrow ADDEDLANE	0%	100%	100%
STOP \rightarrow PEDESTRIAN	0%	100%	100%

was about four meters away from the camera. The experiments were done at noon, at dusk and at night to examine the effects of ambient light on attack efficacy.

The experiments at noon were unsuccessful due to strong sunlight (at illuminance 8×10^4 lux) and our projector was not powerful enough compared with the sunlight. Note that more powerful projectors could be acquired. At dusk when the sunlight’s illuminance went down to 4×10^4 , the patterns in the ghost areas became clear enough to alter the image of the STOP sign. At night when we turned on the vehicle’s front lights, the illuminance at the sign was 30, and the projector was able to shine clear attack patterns.

Table 3 shows the success rates for obfuscation attacks at different times of a day, where the rates were only 30% lower than our in-lab experiments (Fig. 9), when used with our in-lab channel model directly in the road experiments without retraining it. This implies that system-aware attacks are robust against different environments. Moreover, the attack rates on obfuscating some classes (e.g., the STOP sign) into three other signs were 100%, which is critical, as an attacker can easily prevent an autonomous vehicle from stopping at a STOP sign.

Remark: On-road experiment results show that GhostImage attacks are robust to varying environments. The channel model trained indoors can be applied outdoors without retraining.

6.2.3 Different cameras. Previously, we conducted GhostImage attacks on Aptina MT9M034 camera [51] designed for autonomous driving. Here, we evaluate two other cameras, Aptina MT9V034 [52] for autonomous driving as well but with a simpler lens design, and Ring indoor security cameras [63] for surveillance applications.

Aptina MT9V034: We mounted system-aware creation attacks against the same camera-based object classification system as in Section 6.1 but we replaced the camera with the Aptina MT9V034 camera. Since this camera has a smaller aperture size and also a simpler lens design than Aptina MT9M034, for a distance of one meter, only 16×16 -resolution attack patterns could be achieved (previously we had 32×32 at one meter). We did not train a new channel model for this camera, so the attack success rate at one meter was



Figure 12: On-road experiment setup

Table 4: GhostImage untargeted obfuscation attacks against Ring camera on ImageNet dataset in perception domain

Index	Benign Class	Success Rate	Common Prediction
19992	fur boat	100%	geyser, parachute
21539	sunglasses	100%	screen, microwave
22285	sunglasses	100%	plastic bag, geyser
31664	sarong	100%	jellyfish, plastic bag
2849	sweatshirt	100%	laptop, candle
26236	puncho	100%	table lamp

only 75%, which is 25% lower than the Aptina MT9M034 camera. As the distances increased up to four meters, creation attacks yielded success rates as 46.25%, 33.75%, and 12.5%, respectively.

Another reason why the overall success rate was lower is that even though the data sheet of Aptina MT9V034 [52] states that the camera also has the auto exposure control feature, we could not enable the feature in our experiments. In other words, system-aware creation attacks did not benefit from the exposure control. This, on the other hand, demonstrated the robustness of GhostImage attacks: Even without taking advantage of exposure control, the attacks were still effective, with attack success rates as high as 75%.

Ring indoor security camera: We tested GhostImage untargeted attacks against a Ring indoor security camera [63] on the ImageNet dataset. To demonstrate that our attacks can be applied to surveillance scenarios, we assume the camera would issue an intrusion warning if a specific object type [64] is detected by the Inception V3 neural network [75]. The attacker’s goal is to change an object for an intruder class to a non-intruder class. However, we could not find “human”, “person” or “people”, etc. in the output classes, we instead used five human related items (such as sunglasses) as the benign classes. We found six images from the validation set of ImageNet, of which top-1 classification results are one of those five benign classes. The six images were displayed on a monitor. For each benign image, we calculated ten alternative 3×3 attack patterns (the highest resolution at one meter by the Ring camera). Results show that for all six benign images, system-aware attacks achieved untargeted attack success rates of 100% (Table 4), which demonstrates that our attacks can be mounted against applications of not only autonomous driving, but also surveillance systems. Other autonomous systems such as robots and drones may also be vulnerable.

Remark: Results from different cameras demonstrate that GhostImage attacks are robust against varying cameras. The channel model trained on one camera can be transferred to others without retraining because different cameras share similar design principles and parameters. Results from the Aptina MT9V034 camera show that GhostImage attacks can still be effective without exposure control. Results from the Ring camera show that GhostImage attacks can be applied to surveillance scenarios.

7 DISCUSSION

In this section, we discuss practical challenges to GhostImage attacks, speculate as to effective countermeasures, and outline variations on the original attacks.

7.1 Practicality of GhostImage Attacks

There are several challenges an attacker needs to overcome to launch GhostImage attacks. First, the attacks rely largely on ghost effects; if ghosts cannot be induced, or if they are not significant enough, the attacks might be infeasible against a given camera (lens). However, this is unlikely because these effects occur in most cameras (e.g., Apple iPhones [3, 4]). Moreover, no “flare-free” lens exists to the best of our knowledge. In addition, if ghost effects are unavailable to the attacker there are other optics effects available, such as blooming effects [81], that can be leveraged to produce GhostImage-like attacks.

The second challenge regards our assumption concerning the attacker’s knowledge of the camera, i.e., the camera matrix M and color calibration matrix H_c . We note that the attacks can still be *effective* without such knowledge but with it the attacks can be more *efficient*. For example, the attacker may choose to lower their attack success expectation but the probability of successful attack may still be too high for potential victims to bear (e.g., a success rate of only 10% might be unacceptable for reasons of safety in automated vehicles). This challenge can be largely eliminated if the attacker is able to purchase a camera of the same, or similar, model as used in the targeted system and use it derive the matrices. In fact, because of the generality of our channel model the matrices need only be approximate. Lastly, assuming white-box knowledge on sensors is widely adopted and accepted in the literature, e.g., the AdvLiDAR attack [11]. Also, we assume white-box attacks on the neural network, though this assumption can be eliminated by leveraging the transferability of adversarial examples [5, 54, 55].

Thirdly, the overlap of ghosts and objects of interest in images must be nearly complete for the attacks to succeed. In the cases of a moving camera (e.g., one mounted to a vehicle), the attacker needs to be able to accurately track the movement of the targeted camera, otherwise the attacker can only sporadically inject ghosts. We note, however, that the larger the aperture of a camera the larger the ghost(s); additionally, due to the increase in reflection paths, the greater the number of lens in the camera the greater number of ghosts. Taken together these effects increase the probability of successful alignment, even in the case of a moving camera.

The final challenge concerns object detection: we assume that when the object detector crops the image the ghost(s) will be included. Though it cannot be guaranteed that an object detector will inherently include the ghost areas, we point out that a GhostImage attacker could design ghost patterns that cause an object detector to include them [72, 93] and, at the same time, the cropped image would fool subsequent object classification.

7.2 Attack Variations

Should ghosts not be available we have investigated alternative strategies that still allow an attacker to cause misclassification of objects of interest. We prove in Appendix D it is not possible for an attacker to inject adversarial noise, absent ghosts and/or flares, without placing the light source directly in front of the object, which would allow for straightforward detection of the attack.

To allow the attacker to remain concealed we investigated a method in which a beamsplitter merges two light beams coming from two directions: one is the light reflected from the object the

attacker wishes to obscure and the other is the light from the projector. The merged light beams enter the targeted camera as a superposition of the original object and the adversarial pattern, with the resulting image able to fool the image classifier. Appendix F provides details on this attack vector and its efficacy.

Finally, while projectors provide an attacker with the greatest control over adversarial patterns, and hence the ability to spoof complex objects, we have found that RGB lasers [84] can be used at greater distances to spoof simple objects. It may also be possible for an attacker to use multiple laser systems, or even flashlights [12], to create complex patterns akin to the decorative lights displayed on Christmas trees (e.g., <https://linx.li/wl9efae2.jpg>).

7.3 Countermeasures

The most straightforward countermeasure to GhostImage attacks is flare elimination, either by using a lens hood [82, 91] or through flare detection. Lens hoods are generally not favored as they reduce the angle of view of the camera, which is unacceptable for many autonomous vehicle and surveillance applications. While one can try to detect flares/ghosts and eliminate them, they are so common and varied that false negatives inevitably occur and, furthermore, just as adversarial noise can be crafted to deceive neural networks an analogous procedure could be used to craft flares/ghosts that deceive flare/ghost detectors.

A complementary line of defense would be to make neural networks themselves robust to GhostImage attacks. Existing approaches for adversarial examples (e.g., [31, 37, 38, 57]) are ill-suited for this task, however, as GhostImage attacks do not necessarily follow the constraints placed on traditional adversarial examples in that perturbations do not have to be bounded within a small norm.

A partial form of defense may be to exploit prior knowledge, such as GPS locations of signs, to make decisions, instead of just depending on real-time detection (though this approach would not work for spontaneous appearance of objects, e.g., in the context of collision avoidance). Sensor redundancy/fusion could also be helpful: autonomous vehicles could be equipped with multiple cameras and/or other types of sensors, such as LiDARs and radars, which would at least increase the cost of the attack by requiring the attacker to target multiple sensors.

8 RELATED WORK

Since our attack spans two domains, in this section we review both sensor attacks and adversarial examples.

Sensor attacks: Perception in autonomous and surveillance systems occurs through sensors, which convert analog signals into digital ones that are further analyzed by computing systems. Recent work has demonstrated that the sensing mechanism itself is vulnerable to attack and that such attacks may be used to bypass digital protections [21, 89]. For example, anti-lock braking system (ABS) sensors have been manipulated via magnetic fields by Shoukry et al. [68], microphones have been subject to inaudible voice and light-based attacks [74, 92], and light sensors can be influenced via electromagnetic interference to report lighter or darker conditions [65]. The reader is referred to [21] for a comprehensive review of analog sensor attacks.

More closely related to the present work are attacks against LiDAR systems, first discussed in [59, 67], though these works do not consider a neural network backend for object classification. Cao et al. [11] do describe a variant of a LiDAR attack meant to subvert an associated object detection system. We note that LiDAR-based attacks are considerably easier to carry out than our visible light-based attacks against cameras because attackers can directly inject adversarial laser pulses into LiDARs without worrying about blocking the object of interest. Existing attacks against cameras [59, 90] are denial-of-service attacks and do not seek to compromise the object classifier as our GhostImage attacks do. Those attacks that do target object classification [15, 20, 93] are either digital or physical domain attacks (i.e., they need to modify the object of interest, in this case a traffic sign or road pavement, physically or after the object has been captured by a camera) rather than perception domain attacks [21, 89]. Similarly [94] falls within the domain of physical attacks, as opposed to our perception domain attack, as the proposed approach illuminates the object of interest (a human face) with infrared light to fool an infrared-camera. We did not consider infrared noise in our attacks as it can be easily eliminated from visible light systems using infrared filters.

Adversarial examples: State-of-the-art adversarial examples can be categorized as digital or physical domain attacks. In digital domain attacks, the adversarial perturbation is directly applied to images (i.e., at the pixel level). Some of these are white-box attacks in that the adversary knows the architecture and the parameters of the targeted neural network [13, 22, 30, 45, 46, 56, 76, 86]. Others are black-box attacks in which such parameters are unknown [5, 6, 36, 54, 55]. In physical domain attacks objects of interest are physically modified to cause misclassification [20, 30, 66, 69, 94], or to evade detection [28, 85, 93]. These physical domain attacks differ from GhostImage attacks in that we target the sensor (camera) without needing to physically modify any real-world object.

In terms of defending neural networks from adversarial examples, be they physical or digital, schemes include modifying the network to be more robust [10, 19, 22, 31, 35, 38, 57, 60, 83, 87], while other defenses have focused on either detecting adversarial inputs [25, 37, 40, 42, 88] or transforming them into benign images [7, 24, 40].

9 CONCLUSION

In this work we presented GhostImage attacks against camera-based object classifiers. Using common optical effects, viz. lens flare/ghost effects, an attacker is able to inject arbitrary adversarial patterns into camera images using a projector. To increase the efficacy of the attack, we proposed a projector-camera channel model that predicts the location of ghosts, the resolution of the patterns in ghosts, given the relative position of the projector and the camera, and accounts for exposure control and color calibration. GhostImage attacks also leverage adversarial examples to find optimal attack patterns that lead to misclassification desired by the attacker with high confidence. We evaluated GhostImage attacks using three image datasets and in both indoor and outdoor environments on three cameras. Experimental results show that GhostImage attacks were able to achieve attack success rates as high as 100%.

REFERENCES

- [1] Amazon. 2020. Prime Air Delivery. <https://www.amazon.com/Amazon-Prime-Air/b?ie=UTF8&node=8037720011>. (2020).
- [2] Amazon. 2020. Ring. ring.com. (2020).
- [3] Apple. 2017. iPhone 8 Plus horrible lens flare and reflections. <https://discussions.apple.com/thread/8118139>. (2017).
- [4] Apple. 2019. iPhone 11 Pro's irritating lens flare problem. https://www.reddit.com/r/apple/comments/da6qft/iphone_11_pros_irritating_lens_flare_problem/. (2019).
- [5] Arjun Nitin Bhagoji, Warren He, Bo Li, and Dawn Song. 2018. Practical black-box attacks on deep neural networks using efficient query mechanisms. In *European Conference on Computer Vision*. Springer, 158–174.
- [6] Wieland Brendel, Jonas Rauber, and Matthias Bethge. 2018. Decision-based adversarial attacks: Reliable attacks against black-box machine learning models. In *Proceedings of the IEEE conference on learning representations*.
- [7] Jacob Buckman, Aurko Roy, Colin Raffel, and Ian Goodfellow. 2018. Thermometer Encoding: One Hot Way To Resist Adversarial Examples. In *International Conference on Learning Representations*. <https://openreview.net/forum?id=S18Su-CW>
- [8] Minyvonne Burke. 2019. Man hacks Ring camera in 8-year-old girl's bedroom, taunts her: 'I'm Santa Claus'. <https://www.nbcnews.com/news/us-news/man-hacks-ring-camera-8-year-old-girl-s-bedroom-n1100586>. (2019).
- [9] Canon. 2019. Telephoto Zoom EF-S 55-250mm. <https://www.usa.canon.com/internet/portal/us/home/products/details/lenses/ef/telephoto-zoom/ef-s-55-250mm-f-4-5-6-is-ii>. (2019).
- [10] Xiaoyu Cao and Neil Zhenqiang Gong. 2017. Mitigating evasion attacks to deep neural networks via region-based classification. In *Proceedings of the 33rd Annual Computer Security Applications Conference*. ACM, 278–287.
- [11] Yulong Cao, Chaowei Xiao, Benjamin Cyr, Yimeng Zhou, Won Park, Sara Ranzani, Qi Alfred Chen, Kevin Fu, and Z Morley Mao. 2019. Adversarial sensor attack on lidar-based perception in autonomous driving. In *Proceedings of the 2019 ACM SIGSAC Conference on Computer and Communications Security*. ACM, 2267–2281.
- [12] Christian Carlberg. [n. d.]. HexBright, an Open Source Light. <https://www.kickstarter.com/projects/christian-carlberg/hexbright-an-open-source-light>. [n. d.].
- [13] Nicholas Carlini and David Wagner. 2017. Towards evaluating the robustness of neural networks. In *Proceedings of the IEEE Symposium on Security and Privacy*. IEEE, 39–57.
- [14] Stephen Checkoway, Damon McCoy, Brian Kantor, Danny Anderson, Hovav Shacham, Stefan Savage, Karl Koscher, Alexei Czeskis, Franziska Roesner, Tadayoshi Kohno, et al. 2011. Comprehensive experimental analyses of automotive attack surfaces. In *USENIX Security Symposium*, Vol. 4. San Francisco, 447–462.
- [15] Alesia Chernikova, Alina Oprea, Cristina Nita-Rotaru, and Baekgyu Kim. 2019. Are Self-Driving Cars Secure? Evasion Attacks against Deep Neural Networks for Steering Angle Prediction. In *IEEE Security and Privacy Workshop on IoT*. IEEE.
- [16] Andrei Costin, Jonas Zaddach, Aurélien Francillon, and Davide Balzarotti. 2014. A large-scale analysis of the security of embedded firmwares. In *23rd {USENIX} Security Symposium ({USENIX} Security 14)*. 95–110.
- [17] Spencer Cox. 2019. What Is Exposure? (A Beginner's Guide). <https://photographylife.com/what-is-exposure/>. (2019).
- [18] J. Deng, W. Dong, R. Socher, L.-J. Li, K. Li, and L. Fei-Fei. 2009. ImageNet: A Large-Scale Hierarchical Image Database. In *CVPR09*.
- [19] Guneet S. Dhillon, Kamyar Azizzadenesheli, Jeremy D. Bernstein, Jean Kossaifi, Aran Khanna, Zachary C. Lipton, and Animashree Anandkumar. 2018. Stochastic activation pruning for robust adversarial defense. In *International Conference on Learning Representations*. <https://openreview.net/forum?id=H1uR4GZRZ>
- [20] Kevin Eykholt, Ivan Evtimov, Earlene Fernandes, Bo Li, Amir Rahmati, Chaowei Xiao, Atul Prakash, Tadayoshi Kohno, and Dawn Song. 2018. Robust physical-world attacks on deep learning visual classification. In *Proceedings of the IEEE Conference on Computer Vision and Pattern Recognition*. 1625–1634.
- [21] Ilias Giechaskiel and Kasper Bonne Rasmussen. 2020. Taxonomy and Challenges of Out-of-Band Signal Injection Attacks and Defenses. *IEEE Communication Surveys & Tutorials* (2020).
- [22] Ian J Goodfellow, Jonathon Shlens, and Christian Szegedy. 2014. Explaining and harnessing adversarial examples. *arXiv preprint arXiv:1412.6572* (2014).
- [23] Google. 2020. Nest and Google Home. Now under one roof. nest.com. (2020).
- [24] Chuan Guo, Mayank Rana, Moustapha Cisse, and Laurens van der Maaten. 2018. Countering Adversarial Images using Input Transformations. In *International Conference on Learning Representations*. <https://openreview.net/forum?id=SyJ7ClWcb>
- [25] Dan Hendrycks and Kevin Gimpel. 2017. Early Methods for Detecting Adversarial Images.
- [26] Matthias B. Hullin, Elmar Eisemann, Hans-Peter Seidel, and Sungkil Lee. 2011. Physically-Based Real-Time Lens Flare Rendering. *ACM Trans. Graph. (Proc. SIGGRAPH 2011)* 30, 4 (2011), 108:1–108:9.
- [27] Diederik P Kingma and Jimmy Ba. 2015. Adam: A method for stochastic optimization. In *ICLR*.
- [28] Stepan Komkov and Aleksandr Petiushko. 2019. AdvHat: Real-world adversarial attack on ArcFace Face ID system. *arXiv preprint arXiv:1908.08705* (2019).
- [29] Alex Krizhevsky and Geoffrey Hinton. 2009. *Learning multiple layers of features from tiny images*. Technical Report. Citeseer.
- [30] Alexey Kurakin, Ian J Goodfellow, and Samy Bengio. 2018. Adversarial Examples in the Physical World. In *Artificial Intelligence Safety and Security*. Chapman and Hall/CRC, 99–112.
- [31] Mathias Lecuyer, Vaggelis Atlidakis, Roxana Geambasu, Daniel Hsu, and Suman Jana. 2019. Certified robustness to adversarial examples with differential privacy. In *IEEE Symposium on Security and Privacy (S&P)*.
- [32] Hsien-Che Lee. 2005. *Introduction to color imaging science*. Cambridge University Press.
- [33] Sungkil Lee and Elmar Eisemann. 2013. Practical real-time lens-flare rendering. In *Computer Graphics Forum*, Vol. 32. Wiley Online Library, 1–6.
- [34] Qingquan Li, Long Chen, Ming Li, Shih-Lung Shaw, and Andreas Nüchter. 2013. A sensor-fusion drivable-region and lane-detection system for autonomous vehicle navigation in challenging road scenarios. *IEEE Transactions on Vehicular Technology* 63, 2 (2013), 540–555.
- [35] Xuanqing Liu, Minhao Cheng, Huan Zhang, and Cho-Jui Hsieh. 2018. Towards robust neural networks via random self-ensemble. In *Proceedings of the European Conference on Computer Vision (ECCV)*. 369–385.
- [36] Yanpei Liu, Xinyun Chen, Chang Liu, and Dawn Song. 2016. Delving into transferable adversarial examples and black-box attacks. In *Proceedings of the International Conference on Learning Representations*.
- [37] Shiqing Ma, Yingqi Liu, Guan hong Tao, Wen-Chuan Lee, and Xiangyu Zhang. 2019. NIC: Detecting Adversarial Samples with Neural Network Invariant Checking. In *Network and Distributed System Security Symposium*.
- [38] Aleksander Madry, Aleksandar Makelov, Ludwig Schmidt, Dimitris Tsipras, and Adrian Vladu. 2018. Towards Deep Learning Models Resistant to Adversarial Attacks. In *International Conference on Learning Representations*. <https://openreview.net/forum?id=rjzIBfZAb>
- [39] Phil McCausland. 2019. Self-driving Uber car that hit and killed woman did not recognize that pedestrians jaywalk. <https://www.nbcnews.com/tech/tech-news/self-driving-uber-car-hit-killed-woman-did-not-recognize-n1079281>. (2019).
- [40] Dongyu Meng and Hao Chen. 2017. Magnet: a two-pronged defense against adversarial examples. In *Proceedings of the 2017 ACM SIGSAC Conference on Computer and Communications Security*. ACM, 135–147.
- [41] Dr. Meter. 2019. Digital Illuminance Meter. <https://www.amazon.com/gp/product/B07LF4BT8V>. (2019).
- [42] Jan Hendrik Metzen, Tim Genewein, Volker Fischer, and Bastian Bischoff. 2017. On Detecting Adversarial Perturbations. In *Proceedings of the IEEE conference on learning representations*.
- [43] Charlie Miller and Chris Valasek. 2014. A survey of remote automotive attack surfaces. *black hat USA 2014* (2014), 94.
- [44] Andreas Mogelmose, Mohan Manubhai Trivedi, and Thomas B Moeslund. 2012. Vision-based traffic sign detection and analysis for intelligent driver assistance systems: Perspectives and survey. *IEEE Transactions on Intelligent Transportation Systems* 13, 4 (2012), 1484–1497.
- [45] Seyed-Mohsen Moosavi-Dezfooli, Alhussein Fawzi, Omar Fawzi, and Pascal Frossard. 2017. Universal adversarial perturbations. In *Proceedings of the IEEE conference on computer vision and pattern recognition*. 1765–1773.
- [46] Seyed-Mohsen Moosavi-Dezfooli, Alhussein Fawzi, and Pascal Frossard. 2016. Deepfool: a simple and accurate method to fool deep neural networks. In *Proceedings of the IEEE Conference on Computer Vision and Pattern Recognition*. 2574–2582.
- [47] NEC. 2007. *NP Installation Series User's Manual*. NEC. https://www.projectorcentral.com/pdf/projector_manual_3978.pdf
- [48] NEC. 2009. *NP Installation Series Specification Sheet*. NEC. https://www.projectorcentral.com/pdf/projector_spec_3978.pdf
- [49] NEC. 2019. NP05ZL, 4.62" 7.02:1 Zoom Lens. <https://www.necdisplay.com/p/optional-lenses/np05zl>. (2019).
- [50] Nvidia. 2016. *NVIDIA TESLA P100 GPU ACCELERATOR*. Nvidia.
- [51] ON semiconductor. 2017. *MT9M034 1/3-Inch CMOS Digital Image Sensor*. ON semiconductor. <https://www.onsemi.com/pub/Collateral/MT9M034-D.PDF>
- [52] ON semiconductor. 2017. *MT9V034 1/3-Inch Wide-VGA CMOS Digital Image Sensor*. ON semiconductor. <https://www.onsemi.com/pub/Collateral/MT9V034-D.PDF>
- [53] Opteka. 2019. Opteka 650-1300mm Telephoto Zoom Lens. <https://www.amazon.com/Opteka-650-1300mm-1300-2600mm-Telephoto-Digital/dp/B001VDLZIG>. (2019).
- [54] Nicolas Papernot, Patrick McDaniel, and Ian Goodfellow. 2016. Transferability in machine learning: from phenomena to black-box attacks using adversarial samples. *arXiv preprint arXiv:1605.07277* (2016).
- [55] Nicolas Papernot, Patrick McDaniel, Ian Goodfellow, Somesh Jha, Z Berkay Celik, and Ananthram Swami. 2017. Practical black-box attacks against machine learning. In *Proceedings of the 2017 ACM on Asia Conference on Computer and Communications Security*. ACM, 506–519.

[56] Nicolas Papernot, Patrick McDaniel, Somesh Jha, Matt Fredrikson, Z Berkay Celik, and Ananthram Swami. 2016. The limitations of deep learning in adversarial settings. In *2016 IEEE European Symposium on Security and Privacy (EuroS&P)*. IEEE, 372–387.

[57] Nicolas Papernot, Patrick McDaniel, Xi Wu, Somesh Jha, and Ananthram Swami. 2016. Distillation as a defense to adversarial perturbations against deep neural networks. In *Proceedings of the IEEE Symposium on Security and Privacy*. IEEE, 582–597.

[58] Jonathan Petit and Steven E Shladover. 2014. Potential cyberattacks on automated vehicles. *IEEE Transactions on Intelligent Transportation Systems* 16, 2 (2014), 546–556.

[59] Jonathan Petit, Bas Stottelaar, Michael Feiri, and Frank Kargl. 2015. Remote attacks on automated vehicles sensors: Experiments on camera and lidar. *Black Hat Europe 11* (2015), 2015.

[60] Aditi Raghunathan, Jacob Steinhardt, and Percy Liang. 2018. Certified Defenses against Adversarial Examples. In *International Conference on Learning Representations*. <https://openreview.net/forum?id=Bys4ob-Rb>

[61] Joseph Redmon, Santosh Divvala, Ross Girshick, and Ali Farhadi. 2016. You only look once: Unified, real-time object detection. In *Proceedings of the IEEE conference on computer vision and pattern recognition*. 779–788.

[62] Evan Ribnick, Stefan Atev, Osama Masoud, Nikolaos Papanikolopoulos, and Richard Voyles. 2006. Real-time detection of camera tampering. In *2006 IEEE International Conference on Video and Signal Based Surveillance*. IEEE, 10–10.

[63] Ring. 2019. Indoor Security Cameras. <https://shop.ring.com/collections/security-cams#indoor>. (2019).

[64] Ring. 2020. Standard and Advanced Motion Detection Systems Used in Ring Devices. <https://support.ring.com/hc/en-us/articles/115005914666-Standard-and-Advanced-Motion-Detection-Systems-Used-in-Ring-Devices>. (2020).

[65] Jayaprakash Selvaraj, Gökçen Y Dayanıklı, Neelam Prabhu Gaunkar, David Ware, Ryan M Gerdes, Mani Mina, et al. 2018. Electromagnetic induction attacks against embedded systems. In *Proceedings of the 2018 on Asia Conference on Computer and Communications Security*. ACM, 499–510.

[66] Mahmood Sharif, Sruti Bhagavatula, Lujo Bauer, and Michael K Reiter. 2016. Accessorize to a crime: Real and stealthy attacks on state-of-the-art face recognition. In *Proceedings of the 2016 ACM SIGSAC Conference on Computer and Communications Security*. ACM, 1528–1540.

[67] Hocheol Shin, Dohyun Kim, Yujin Kwon, and Yongdae Kim. 2017. Illusion and dazzle: Adversarial optical channel exploits against lidars for automotive applications. In *International Conference on Cryptographic Hardware and Embedded Systems*. Springer, 445–467.

[68] Yasser Shoukry, Paul Martin, Paulo Tabuada, and Mani Srivastava. 2013. Non-invasive spoofing attacks for anti-lock braking systems. In *International Workshop on Cryptographic Hardware and Embedded Systems*. Springer, 55–72.

[69] Chawin Sitawarin, Arjun Nitin Bhagoji, Arsalan Mosenia, Prateek Mittal, and Mung Chiang. 2018. Rogue signs: Deceiving traffic sign recognition with malicious ads and logos. In *IEEE Security and Privacy Workshop on Deep Learning and Security*. IEEE.

[70] Skydio. 2020. Skydio 2. skydio.com. (2020).

[71] Yunmok Son, Hocheol Shin, Dongkwan Kim, Youngseok Park, Juhwan Noh, Kibum Choi, Jungwoo Choi, and Yongdae Kim. 2015. Rocking drones with intentional sound noise on gyroscopic sensors. In *24th {USENIX} Security Symposium ({USENIX} Security 15)*. 881–896.

[72] Dawn Song, Kevin Eykholt, Ivan Evtimov, Earlene Fernandes, Bo Li, Amir Rahmati, Florian Tramer, Atul Prakash, and Tadayoshi Kohno. 2018. Physical adversarial examples for object detectors. In *12th {USENIX} Workshop on Offensive Technologies ({WOOT} 18)*.

[73] Benjamin Steinert, Holger Dammert, Johannes Hanika, and Hendrik PA Lensch. 2011. General spectral camera lens simulation. In *Computer Graphics Forum*, Vol. 30. Wiley Online Library, 1643–1654.

[74] Takeshi Sugawara, Benjamin Cyr, Sara Rampazzi, Daniel Genkin, and Kevin Fu. [n. d.]. Light Commands: Laser-Based Audio Injection Attacks on Voice-Controllable Systems. ([n. d.]).

[75] Christian Szegedy, Vincent Vanhoucke, Sergey Ioffe, Jon Shlens, and Zbigniew Wojna. 2016. Rethinking the inception architecture for computer vision. In *Proceedings of the IEEE conference on computer vision and pattern recognition*. 2818–2826.

[76] Christian Szegedy, Wojciech Zaremba, Ilya Sutskever, Joan Bruna, Dumitru Erhan, Ian Goodfellow, and Rob Fergus. 2014. Intriguing properties of neural networks. In *ICLR*.

[77] Richard Szeliski. 2010. *Computer vision: algorithms and applications*. Springer Science & Business Media.

[78] Tesla. 2020. Autopilot. <https://www.tesla.com/autopilot>. (2020).

[79] Uber. 2020. Self-Driving Car Technology by Uber. <https://www.uber.com/us/en/atg/technology/>. (2020).

[80] Waymo. 2020. Waymo. <https://en.wikipedia.org/wiki/Waymo>. (2020).

[81] Wikipedia. 2020. Bloom (shader effect). [https://en.wikipedia.org/wiki/Bloom_\(shader_effect\)](https://en.wikipedia.org/wiki/Bloom_(shader_effect)). (2020).

Table 5: Neural network architecture for LISA dataset

Layer Type	Model
ReLU convolution	64 8×8 -filters
ReLU convolution	128 6×6 -filters
ReLU convolution	128 5×5 -filters
ReLU Fully-connected	256
Softmax	8

Table 6: Balanced LISA dataset

Index	Sign Name	Quantity
0	Added Lane	80
1	Merge	80
2	Pedestrian Crossing	80
3	School	77
4	Signal Ahead	80
5	Stop	80
6	Stop Ahead	80
7	Yield	80

[82] Wikipedia. 2020. Lens Hood. en.wikipedia.org/wiki/Lens_hood. (2020).

[83] Eric Wong and J Zico Kolter. 2018. Provable defenses against adversarial examples via the convex outer adversarial polytope. In *International Conference on Machine Learning*.

[84] Laser World. [n. d.]. RGB Laser. <https://www.laserworld.com/en/show-laser-light-faq/glossary-definitions/88-r/2549-rgb-laser.html>. ([n. d.]).

[85] Zuxuan Wu, Ser-Nam Lim, Larry Davis, and Tom Goldstein. 2019. Making an invisibility cloak: Real world adversarial attacks on object detectors. *arXiv preprint arXiv:1910.14667* (2019).

[86] Chaowei Xiao, Jun-Yan Zhu, Bo Li, Warren He, Mingyan Liu, and Dawn Song. 2018. Spatially transformed adversarial examples. In *Proceedings of the IEEE conference on learning representations*.

[87] Cihang Xie, Jianyu Wang, Zhishuai Zhang, Zhou Ren, and Alan Yuille. 2018. Mitigating Adversarial Effects Through Randomization. In *International Conference on Learning Representations*. <https://openreview.net/forum?id=Sk9yqu10Z>

[88] Weilin Xu, David Evans, and Yanjun Qi. 2018. Feature Squeezing: Detecting Adversarial Examples in Deep Neural Networks. In *Network and Distributed Systems Security Symposium (NDSS)*.

[89] C. Yan, H. Shin, C. Bolton, W. Xu, Y. Kim, and K. Fu. 2020. SoK: A Minimalist Approach to Formalizing Analog Sensor Security. In *2020 IEEE Symposium on Security and Privacy (SP)*. IEEE Computer Society, Los Alamitos, CA, USA, 480–495. <https://doi.org/10.1109/SP.2020.00026>

[90] Chen Yan, Wenyuan Xu, and Jianhao Liu. 2016. Can you trust autonomous vehicles: Contactless attacks against sensors of self-driving vehicle. *DEF CON 24* (2016).

[91] Yaopey. 2019. How To Deal With Lens Flare. www.fotographee.com/how-to-deal-with-lens-flare. (2019).

[92] Guoming Zhang, Chen Yan, Xiaoyu Ji, Tianchen Zhang, Taimin Zhang, and Wenyuan Xu. 2017. DolphinAttack: Inaudible Voice Commands. In *Proceedings of the 2017 ACM SIGSAC Conference on Computer and Communications Security (CCS '17)*. Association for Computing Machinery, New York, NY, USA, 1033–1117. <https://doi.org/10.1145/3133956.3134052>

[93] Yue Zhao, Hong Zhu, Ruigang Liang, Qintao Shen, Shengzhi Zhang, and Kai Chen. 2019. Seeing isn’t Believing: Towards More Robust Adversarial Attack Against Real World Object Detectors. In *Proceedings of the 2019 ACM SIGSAC Conference on Computer and Communications Security*. ACM, 1989–2004.

[94] Zhe Zhou, Di Tang, Xiaofeng Wang, Weili Han, Xiangyu Liu, and Kehuan Zhang. 2018. Invisible mask: Practical attacks on face recognition with infrared. *arXiv preprint arXiv:1803.04683* (2018).

A NEURAL NETWORKS AND DATASETS

Here we present the architectures of two neural networks (Tables 5 and 7) and their hyper-parameters (Table 8). The balanced LISA dataset is also detailed in Table 6.

Table 7: Neural network architecture for CIFAR-10 dataset

Layer Type	Model
ReLU convolution	64 8×8 -filters
ReLU convolution	128 6×6 -filters
ReLU convolution	128 5×5 -filters
ReLU convolution	64 3×3 -filters
Max Pooling	2×2
ReLU convolution	128 3×3 -filters
ReLU convolution	128 3×3 -filters
Max Pooling	2×2
ReLU Fully-connected	256
ReLU Fully-connected	256
Softmax	10

Table 8: Training hyper-parameters

Parameter	Value
Learning Rate	0.1
Momentum	0.9
Dropout	0.5
Batch Size	128
Epochs	50

Table 9: Channel model parameter examples

Description	Symbol	Value
Throwing ratio	r_{throw}	20
Physical size of ghosts	S_f	0.0156 cm^2
Projection resolution	P_O	1024×768
Flare booster	ρ	30
Bulb intensity	T_a	$[0, 1]$
Ambient illuminance	\mathcal{I}_{env}	0.02 (indoor)
Projector Max ill.	\mathcal{I}_{max}	1200 (at 1 m)
Camera matrix	M	See below
Color calibration matrix	H_c	See below
In Equation 6	a	8.9
In Equation 6	b	6.7
In Equation 6	c_t	-7.8
In Equation 6	c_d	0.25

B CHANNEL MODEL RESULTS

Table 9 lists all parameters of the projector-camera channel model.

The color calibration matrix is

$$H_c = \begin{bmatrix} 0.5 & 0 & 0.1 \\ 0 & 0.5 & 0 \\ 0 & 0 & 0.8 \end{bmatrix}.$$

The camera matrix is

$$M = \begin{bmatrix} -0.1406 & 0.0537 & -0.0200 & 0.8452 \\ 0.0321 & 0.0547 & -0.1385 & 0.4893 \\ -0.0000 & -0.0000 & -0.0000 & 0.0009 \end{bmatrix}.$$

C SYSTEM-AWARE ATTACK ILLUSTRATIONS

Biased penalty and grid patterns are illustrated in Figure 17 and Figure 18, respectively.

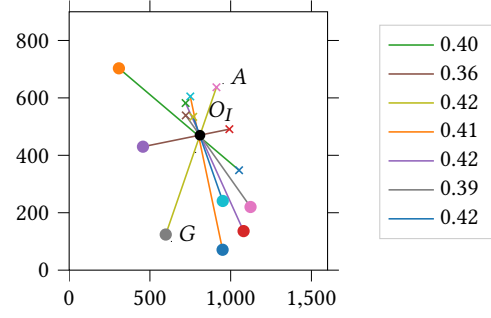


Figure 13: Ghost position v.s. light source position. Crosses are light source at different locations and the circles are the according ghosts.

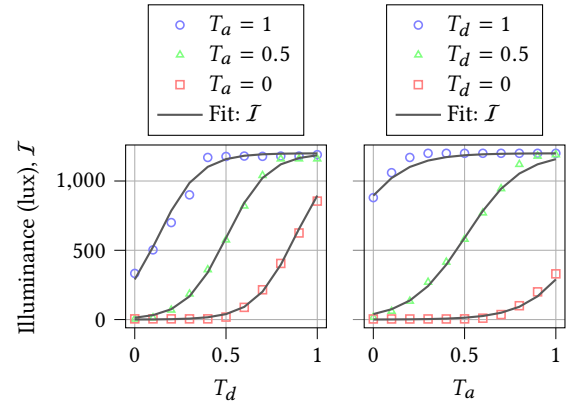


Figure 14: Illuminance depends on the RGB amplitude T_d , and the light bulb intensity T_a .

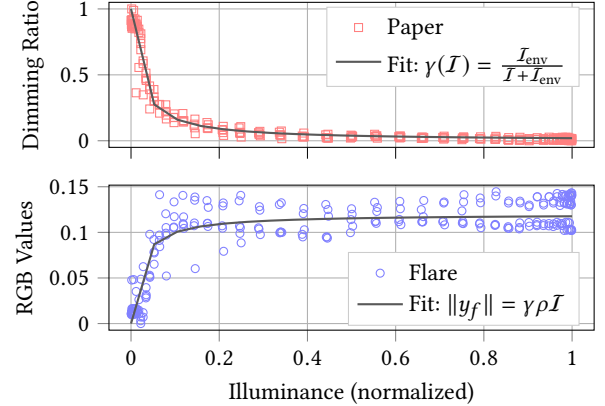
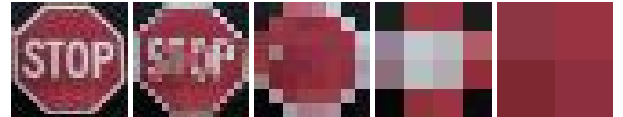


Figure 15: Perceived RGB values v.s. illuminance.



(a) 32×32 (b) 16×16 (c) 8×8 (d) 4×4 (e) 2×2

Figure 16: Downsampling examples. We actually upsampled these images for the sake of presentation, otherwise they were too tiny to show.

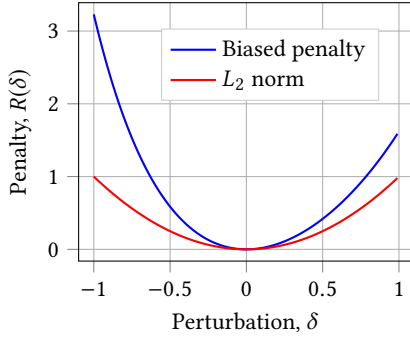


Figure 17: Biased penalty

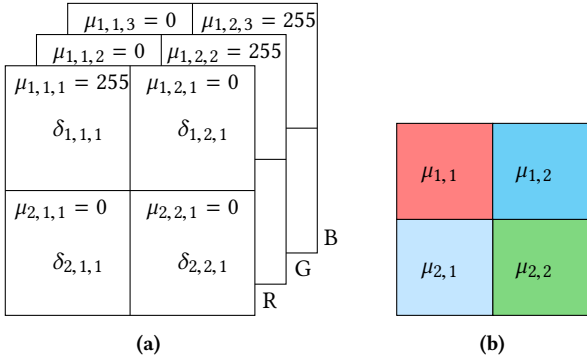


Figure 18: A grid pattern when $N_{row} = N_{col} = 2$ and $N_{chn} = 3$. (a) μ is a three-dimensional matrix. (b) The resulting perturbation pattern.

D DIRECT PROJECTION USING AN ADDITIONAL LENS

LEMMA D.1. *However the additional lenses are placed, the image of noise cannot overlay with the image of the object without obscuring the object.*

PROOF. We are going to prove that even with an additional concave lens. See Figure 19 for a diagram, where a concave lens L_1 is placed between an object AB and a camera's convex lens L_2 . L_1 's focal length is f_1 and L_2 's is f_2 . The distance between L_1 and L_2 is d_2 . The noise source N is right upon A . From the perspective of L_2 , AB is completely obfuscated by L_1 ; in other words, all light rays of AB that go through L_2 must at first go through L_1 . Both the object and the noise source share the same object distance to L_1 , which is d_1 . The image of AB formed by L_1 is A_1B_1 , and N_1 is the image of N . The distance between A_1B_1 and L_1 is d_3 . The image of formed by L_2 is A_2B_2 and N_2 . The distance between A_2B_2 and L_2 is d_4 .

In order to solve a problem consisting of multiple lenses, we usually analyze each lens individually and sequentially. That is, we calculate the image formed by the first lens, then use that image as the input to the second lens.

For L_1 , the input is AB , thus we have

$$\frac{1}{d_1} + \frac{1}{d_3} = \frac{1}{f_1}, \quad (18)$$

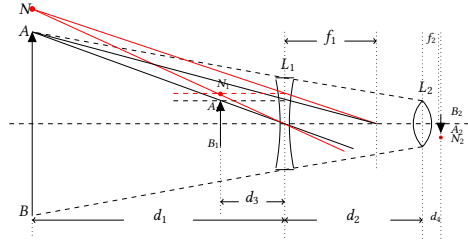


Figure 19: Noise N cannot overlap with the image of the object AB even with an additional concave lens.

and the magnification is calculated as

$$M = \frac{|N_1B_1|}{|NB|} = \frac{|A_1B_1|}{|AB|} = \frac{|A_1N_1|}{|AN|} = \frac{d_3}{d_1}, \quad (19)$$

from which we know that N_1 does not overlap with A_1B_1 .

For L_2 , the input is A_1B_1 (L_2 cannot "see" AB directly because AB is completely obfuscated by L_1), thus we get

$$\frac{1}{d_2 + d_3} + \frac{1}{d_4} = \frac{1}{f_2}, \quad (20)$$

and the magnification is calculated as

$$M = \frac{|N_2B_2|}{|N_1B_1|} = \frac{|A_2B_2|}{|A_1B_1|} = \frac{|A_2N_2|}{|A_1N_1|} = \frac{d_4}{d_2 + d_3}, \quad (21)$$

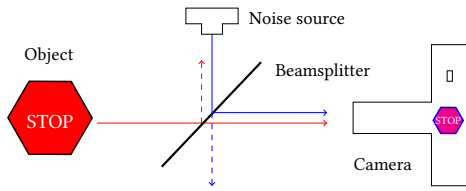
from which we know that N_2 does not overlap with A_2B_2 . As a result, no matter how we place the additional concave lens, we cannot apply the noise to the image of the object without obscuring the object. The proof for a convex lens follows the same logic. \square

E GHOSTIMAGE ATTACK EVALUATION PROCEDURE

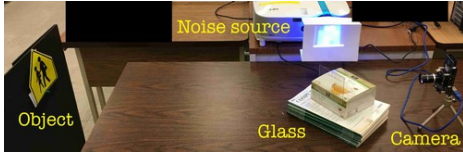
See Algorithm 1.

Algorithm 1: GhostImage Attack evaluation procedure (m : number of classes)

- 1 Initialize $q_d = 0$, for $1 \leq d \leq 5$
 - 2 **for** $d = 1 \dots 5$ **do**
 - 3 Place camera d meters away from projector
 - 4 **for** $i = 1 \dots m$ **do**
 - 5 Place printed traffic sign of class i at background
 - 6 **for** $j = 1 \dots m$ **do**
 - 7 **if** $i = j$ **then** continue
 - 8 $Y \leftarrow k$ randomly picked images of class j from LISA
 - 9 **for** $y \in Y$ **do**
 - 10 Downsample y according to Eq. (3)
 - 11 Project and crop out y'
 - 12 **if** y' is classified as j **then**
 - 13 $q_d \leftarrow q_d + 1$
 - 14 Success rates: $q_d \leftarrow q_d / (km^2)$, for $1 \leq d \leq 5$
-



(a) Noise injection with a beam-splitter/glass



(b) Experiment setup with a piece of glass.

Figure 20: The beamsplitter method setup.

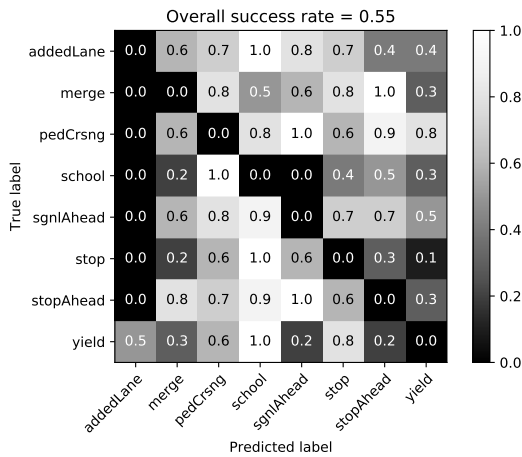


Figure 21: Misclassification matrix of the beamsplitting method at 4×4 resolutions

F BEAMSPLITTING METHOD

See Figure 20a for a diagram of this method, where a beamsplitter is used to merge two light beams coming from two directions. The light beams coming from the object (marked in red) get reflected and transmitted, i.e., the beamsplitter does not obscure the object. The transmitted portions go into the camera, forming an image of the object. The light beams from the light noise source (marked in blue) also get reflected and transmitted. The reflected portions (instead of the transmitted portions) are captured by the camera, forming an image of the noise. Two images overlap as a potential adversarial example, depicted as a small magenta (red plus blue) stop sign in the camera.

An in-lab experimental setup is shown in Figure 20b. In this setup, we used the NEC projector [48] as the light noise source. Instead of using an expensive beamsplitter, we found out that a single piece of glass could also function like a beamsplitter. We placed a piece of white paper in front of the projector’s lens to reduce the projected image size (otherwise the projected image becomes too large even within a small throwing distance). This does not change the attack plausibility because the imager can clearly capture the noise pattern on the paper. These elements were placed in a way that the noise image (from the paper) would overlap with the image of the object from the view of the camera. a misclassification matrix is shown in Figure 21 where an overall attack success rate of 55% was achieved.